JOURNAL OF GEOPHYSICAL RESEARCH, VOL. 106, NO. D19, PAGES 22,991–23,007, OCTOBER 16, 2001

Nonequilibrium coexistence of solid and liquid particles in Arctic stratospheric clouds

J. Biele,[1,2] A. Tsias,[3,4] B. P. Luo,[5,4] K. S. Carslaw,[6,4] R. Neuber,[7]
G. Beyerle,[8,2] T. Peter [5,4]

Abstract. Observations of polar stratospheric clouds (PSCs) from Ny Ålesund, Spitsbergen, have been examined to quantify the occurrence of solid particles. The polarized backscatter ratio was found to be a more sensitive indicator of the presence of non-spherical (solid) particles in a PSC than the aerosol depolarization, which approaches zero for clouds containing a large volume of liquid droplets. The analysis corroborates our previous finding that type Ia PSCs cannot be composed of nitric acid trihydrate particles in equilibrium with the gas phase, which would lead to a much too high backscatter ratio. Conversely, type Ib PSCs, previously thought to be composed solely of liquid droplets, often contain a very small fraction of solid particles. These clouds develop a high parallel backscatter, arising from Mie scattering by droplets, and a nonvanishing perpendicular signal due to the few solid particles. Other type Ib PSCs appear to contain only liquid particles. The mixed liquid/solid clouds are observed on the smallest spatial and temporal scale resolvable by the lidar instrument (30 m, 1 min), implying that their properties are not a result of spatial averaging of different cloud types. Comparison of the observations with optical calculations shows that such nonequilibrium particle distributions are to be expected, as temperature changes are sufficiently rapid to prevent the particles from assuming equilibrium sizes. The observed optical characteristics of type Ia and type Ib clouds can be reproduced in a model by assuming that a very small fraction of the particles are composed of nitric acid hydrate, with the majority being binary H_2SO_4/H_2O or ternary $HNO_3/H_2SO_4/H_2O$ droplets.

1. Introduction

The understanding of polar stratospheric ozone loss depends crucially on our knowledge of polar stratospheric cloud (PSC) properties [World Meteorological Organization (*WMO*), 1994]. The information required includes their geographical and vertical extent, the chemical composition and phase of the cloud particles, their surface area and volume densities, the duration of individual PSC events, and their ability to denitrify stratospheric air by sedimentation. Our capability to predict these properties from given meteorological and chemical conditions (temperature, pressure, winds, concentration of trace gases) is still very limited. Improvements of our prognostic capabilities concerning future ozone loss [e.g., *Shindell et al.*, 1998; *Waibel et al.*, 1999] rely on a comprehensive understanding of the available data sets. The present study is based on a subset of lidar data from Ny Ålesund, which comprise one of the longest and most extensive time series of PSC observations.

The denitrification potential of PSCs is governed by the question of how sufficiently large HNO_3-containing particles can form [e.g., *Waibel et al.*, 1999; *Fahey et al.*, 2001]. Such particles must be solid and must occur in small number densities, as HNO_3 uptake by the numerous liquid particles does not allow particles to grow sufficiently large for rapid sedimentation. Hence a central question is how liquid particles convert into solid particles and whether they can coexist in PSCs. Such coexistence can either be thermodynamic in nature; that is, the mixed particles are in equilibrium and can coexist

[1]Deutsches Zentrum für Luft- und Raumfahrt, Cologne, Germany.
[2]Previously at Alfred Wegener Institute, Potsdam, Germany.
[3]Airsys ATM, Langen, Germany.
[4]Previously at Max Planck Institute for Chemistry, Mainz, Germany.
[5]Laboratorium für Atmosphärenphysik, Swiss Federal Institute of Technology, Zürich, Switzerland.
[6]School of the Environment, University of Leeds, Leeds, England.
[7]Alfred Wegener Institute for Polar and Marine Research, Research Unit Potsdam, Germany.
[8]GeoForschungsZentrum, Potsdam, Germany.

Paper number 2001JD900188.
0148-0227/2001JD900188$09.00

forever [*Koop et al.*, 1997], or it can be kinetic; that is, the atmosphere does not allow for sufficient time to let one particle class evaporate in favor of another. While the thermodynamic coexistence, e.g., between ice particles and H_2SO_4/H_2O droplets, plays a large role in atmospheric processes, it is especially the nonequilibrium (kinetically controlled) coexistence between ternary solution droplets ($HNO_3/H_2SO_4/H_2O$) and the thermodynamically stable nitric acid hydrate particles which governs the denitrification potential. *Shibata et al.* [1997, 1999a b] and *Deshler et al.* [2000] reported on the possible coexistence of solid and liquid HNO_3-containing particles in individual cloud observations, and the former authors also simulate these coexisting states by means of a coupled microphysical and optical model. In the present paper we corroborate and extend their findings: we use the Ny Ålesund lidar data as a statistical basis and highlight the value of the perpendicular backscatter ratio to identify solid particles; and combining these data with microphysical/optical modeling, we show the nonequilibrium coexistence of solid and liquid particles to be a common state in the Arctic.

Such kinetic or nonequilibrium effects may be caused by gas phase diffusion impedance and surface accommodation impedance, which hinder the establishment of equilibrium conditions between the gas phase and the numerous supercooled ternary solution (STS) particles on the one hand and the very few hydrate particles on the other hand. Indeed, it may take hours or days until the hydrate particles have absorbed the HNO_3 that is available for them according to thermodynamic equilibrium considerations.

Lidar systems are well suited for systematically probing PSCs, in particular, when using depolarization of the lidar signal to detect nonspherical (i.e.,, presumably solid) particles. A distinction of two major classes of PSCs, types I and II, was first made based on lidar measurements by *Poole and McCormick* [1988]. Lidar measurements by *Browell et al.* [1990] allowed *Toon et al.* [1990] to further distinguish between type Ia PSCs with high aerosol depolarization ($\delta^{\mathrm{Aer}} = 30$–$50\%$) and low total backscatter ratio ($S_t < 1.5$) and type Ib PSCs with high total backscatter ratio ($S_t > 2$–3) but low depolarization ($\delta^{\mathrm{Aer}} < 3\%$). In comparison, type II PSCs are characterized by much higher backscatter ratios and aerosol depolarizations ($S_t > 7$ and $\delta^{\mathrm{Aer}} > 10\%$). All of these values have been recalculated for 532 nm from the 603-nm wavelength of the *Browell et al.* [1990] lidar data using their measured wavelength dependence of S_t.

While it is clear that type II PSCs must consist of water ice, composition and phase of type I PSCs are still under debate. As has been argued by *Toon et al.* [1990], type Ia PSCs may be explained in terms of clouds consisting of a few relatively large aspherical particles, most likely composed of nitric acid trihydrate (NAT). Such particles should result in high aerosol depolarization but low backscatter ratio and may exist at temperatures below T_{NAT}, the NAT equilibrium temperature [*Hanson and Mauersberger*, 1988]. However, as we show here for the first time, a crucial prerequisite for obtaining $S_t < 1.5$ is that the total condensed mass in these clouds must be less than the total HNO_3 available, corroborating an interpretation by *Peter* [1997] of in situ particle measurements. This is severely restricting the cloud particle number densities encountered in type Ia PSCs.

Type Ib clouds were originally identified by *Toon et al.* [1990] to be composed of a large number of small particles, spherical or almost spherical in shape, but most likely solid. Later, thermodynamic models of supercooled ternary solutions offered a robust explanation for type Ib PSCs in terms of $HNO_3/H_2SO_4/H_2O$ droplets [*Carslaw et al.*, 1994; *Tabazadeh et al.*, 1994]. Such models predicted coupled HNO_3/H_2O uptake by the small background liquid H_2SO_4/H_2O aerosol particles below the temperature T_{STS}, the so-called "dew point" of STS (under conditions typical for the lower stratosphere it is $T_{\mathrm{STS}} \approx T_{\mathrm{NAT}} - 3.6$ K [*Biele*, 1999]). Thus the models suggested type Ib PSCs to be mostly liquid and successfully explained several in situ and remote PSC measurements within the uncertainties [e.g., *Carslaw et al.*, 1994; *Beyerle et al.*, 1997; *Hervig et al.*, 1997]. Although this concept explains most features of type Ib PSCs, we will show in this work that type Ib clouds may often contain solid particles in low number densities, whose optical properties are masked by the large number of relatively large droplets.

In addition, a series of other observations have been made that do not fit directly into the scheme of type II, Ia, and Ib PSCs. On the basis of balloon-borne backscatter sonde data, *Rosen et al.* [1997] suggested the existence of a PSC type whose optical properties could be explained in terms of a mixture of type Ia and type Ib and termed these as type M (standing for mixture). On the basis of the optical specification specification given by Rosen *et al.* [1997], it is conceivable that these clouds are type Ib clouds with a small fraction of solid particles, which we discuss in detail below. On the basis of lidar data from Sodankylä (Finland), an apparently new type (which had been tentatively called type Id), has recently been described by *Wedekind* [1997] and *Stein et al.* [1999]. This cloud type is optically characterized by high aerosol depolarizations ($\delta^{\mathrm{Aer}} = 10$–$30\%$) combined with moderately high backscatter ratio ($S_t = 2$–4 for 532 nm). A more comprehensive study by *Tsias et al.* [1999] shows that the same type of cloud has also been observed in the recent Airborne Polar Experiment APE-POLECAT (Polar Stratospheric Clouds, Lee waves, Chemistry, Aerosols, and Transport) campaign using airborne lidar and that it may occur under rare circumstances at all European lidar stations (including the Sodankylä data discussed by Wedekind or Stein *et al.* and the Ny Ålesund data discussed here). *Tsias et al.* [1999] showed that these clouds may be explained as type Ia clouds with a higher degree of HNO_3 hydrate

particle activation (leading to an enhanced backscatter ratio) than is the case in a standard type Ia cloud (while particle radii appear to be similar). Accordingly, such enhanced Ia clouds have been termed type Ia-enh by *Tsias et al.* [1999]. In contrast to regular type Ia clouds, kinetic calculations of the formation process of type Ia-enh require typically 10–50% of particle activation. Recently, *Toon et al.* [2000] described lidar observations of many small solid particles in January 1989 and termed them type Ic (not to be confused with the metastable amorphous solids once hypothesized by *Tabazadeh and Toon* [1996], which were also called type Ic). We note that the characteristics of these clouds are very similar to the type Ia-enh described above.

In the present paper, using the Ny Ålesund lidar observations combined with microphysical/optical modeling, we address the very nature of type I PSCs in a general sense: what fraction of the available HNO_3 is contained in type Ia PSCs, and do type Ib PSCs consist only of spherical (presumably liquid) particles?

2. Experimental Section

2.1. Instrumental Setup

The observations presented here were performed with the Alfred Wegener Institute's multiwavelength and polarization aerosol lidar instrument at the Primary Arctic Station of the Network for the Detection of Stratospheric Change (NDSC) in Ny Ålesund, Spitsbergen (79°N, 12°E). For a comprehensive description, see *Biele et al.* [1997a, b], *Biele* [1999], *Stebel et al.* [1996], or *Beyerle et al.* [1994]. The polarization measurements utilize the second harmonic of a Nd:YAG laser at a wavelength of $\lambda = 532$ nm operating with a pulse repetition frequency of 30 Hz. Laser pulse energy is 180 mJ, typically. The signals backscattered from the atmosphere are collected with a 60-cm telescope (field of view $\alpha = 0.8$ mrad), separated according to wavelength and perpendicular/parallel polarization and detected by sensitive photomultipliers in photon-counting mode. A mechanical chopper prevents saturation of the photodetectors by signals from low altitudes. The instrument was refined and improved several times in recent years. The highest resolution attainable is 1 min in time and 15 to 30 m in altitude.

In this work we analyze the 532-nm polarized return. Two polarizing beam splitters are used to separate the two polarization directions parallel ($\parallel$) and perpendicular ($\perp$) with respect to the plane of polarization of the emitted beam, respectively. For the winter 1996/1997, only one beam splitter was used with implications for instrumental bias as we will discuss below. Interference filters with a full width at half maximum (FWHM) of 10 nm are used to suppress stray light. The resulting bandwidth implies a molecular depolarization of the Rayleigh atmosphere (i.e., purely molecular atmosphere without particulates) of $\delta^{\mathrm{Ray}} = 1.44\%$ at 532 nm.

2.2. Observables

We present measurements of the parallel, perpendicular, and total backscatter ratios

$$S_{\parallel,\perp,t} = \frac{\beta^{\mathrm{Ray}}_{\parallel,\perp,t} + \beta^{\mathrm{Aer}}_{\parallel,\perp,t}}{\beta^{\mathrm{Ray}}_{\parallel,\perp,t}}, \tag{1}$$

which are defined in terms of the parallel, perpendicular and total backscatter coefficients $\beta_{\parallel}$, $\beta_{\perp}$, and $\beta_t = \beta_{\parallel} + \beta_{\perp}$, respectively. In addition, we use volume depolarization δ^{Vol} and aerosol depolarization δ^{Aer}:

$$\delta^{\mathrm{Vol}} = \frac{\beta_{\perp}}{\beta_{\parallel}}, \tag{2a}$$

$$\delta^{\mathrm{Vol}} = \frac{S_{\perp}}{S_{\parallel}}\,\delta^{\mathrm{Ray}}, \tag{2b}$$

$$\delta^{\mathrm{Aer}} = \frac{\beta^{\mathrm{Aer}}_{\perp}}{\beta^{\mathrm{Aer}}_{\parallel}} = \frac{S_{\perp} - 1}{S_{\parallel} - 1}\,\delta^{\mathrm{Ray}}, \tag{3}$$

with $\delta^{\mathrm{Ray}} = \beta^{\mathrm{Ray}}_{\perp}/\beta^{\mathrm{Ray}}_{\parallel} \approx 0.0144$.

Low aerosol contents render the calculation of δ^{Aer} difficult because the uncertainty diverges as $S_{\parallel} \to 1$. Under these circumstances, δ^{Aer} is not an ideal observational variable for describing optical properties of PSCs. Even though ($S_{\perp}$, δ^{Aer}) and ($S_{\perp}$, $S_{\parallel}$) mathematically contain the same information, the latter set of observables is the better choice for judging the properties of aerosol ensembles.

2.3. Processing of Data

For the current application, raw data have been binned into 1-hour time intervals and 200-m height intervals. Nonlinearities of the detection system ("dead time effects," pulse pileup) were removed using the method described by *Donovan et al.* [1993] and *Steinbrecht* [1994]. The relevant constants have been measured (winter 1996/1997 [see *Biele*, 1999]) or estimated (previous winters). Note that these corrections are small compared to the signal's statistical uncertainty. Background count rates were subtracted after verification that signal-induced noise was negligible by imposing a constraint on the maximum admissible count rate. Uncertainties were computed assuming Poisson statistics for the statistical errors; systematic errors were calculated from the uncertainties of the nonlinearity correction, the measured air density, and the ratio of extinction to backscatter coefficients for aerosol particles, $L = \alpha^{\mathrm{Aer}}/\beta^{\mathrm{Aer}} = 40$ sr. This is assumed to be constant in both time and altitude, and because the exact value is not known, we assume a relative error of 50%. The resulting uncertainty in backscatter coefficients is usually <10% of the statistical error of the signal since type I PSCs are optically thin. The total backscatter ratio S_t was computed by adding first the intensities of the two polarized channels; then all

three backscatter coefficients and ratios $(\|, \perp, t)$ were calculated by Klett's method [*Klett*, 1981; 1985; *Biele*, 1999]. The necessary normalization to $S_{\|,\perp,t} = 1$ was performed in the aerosol-free atmosphere above $\geq$26 km where we never detected aerosols, using the value of the Rayleigh depolarization ($\delta^{\mathrm{Ray}} = 1.44\%$). We used measured ozone densities (from at least weekly ozone sondes at Ny Ålesund) and absolute ozone absorption cross sections [*Burrows et al.*, 1999] to correct for ozone absorption. Frequent (up to three per day) local meteorological radio sondes (pressure, temperature and humidity) deliver profiles that have been interpolated linearly in time in order to derive air density.

2.4. A Posteriori Corrections of Polarized Quantities

Difficulties in obtaining precise depolarization measurements are often underestimated. Instrumental contributions to an erroneous depolarization measurement can be summarized as follows: (1) intrinsic laser depolarization, i.e., incomplete polarization of the emitted laserlight; (2) faulty alignment of the detector polarization plane with respect to the emitter polarization plane; (3) imperfect separation or "cross talk" of the two polarization directions in the detector.

The analysis of data processed as described in the previous subsection still showed some cross talk between the $\|$ and $\perp$ channels, as is apparent from a usually slight linear increase in $S_\perp$ with $S_\|$; that is, a strong parallel backscatter signal strays into the perpendicular channel. An appropriate correction is of particular importance in the present context. An explanation and an a posteriori correction of this phenomenon have been described by *Baumgarten* [1997]. Generalizing this work [*Biele and Beyerle*, 2000], we obtain the following corrections (the superscript "meas" is used to distinguish the uncorrected from corrected quantities):

$$S_\| \cong S_\|^{\mathrm{meas}}, \tag{4}$$

$$S_\perp = \left(1 + \frac{\delta^c}{\delta^{\mathrm{Ray}}}\right) S_\perp^{\mathrm{meas}} - \frac{\delta^c}{\delta^{\mathrm{Ray}}} S_\|^{\mathrm{meas}}, \tag{5}$$

$$\delta^{\mathrm{Aer}} = \left(1 + \frac{\delta^c}{\delta^{\mathrm{Ray}}}\right) \delta^{\mathrm{Aer,meas}} - \delta^c, \tag{6}$$

$$\delta^{\mathrm{Vol}} = \frac{S_\perp}{S_\|}\, \delta^{\mathrm{Ray}}, \tag{7}$$

with a single constant δ^c describing all instrumental contributions mentioned above. Here δ^{Vol} is implicitly corrected since it is calculated from already corrected quantities. Note that errors due to cross talk in $S_\|$ ($S_\perp$) are proportional to the absolute value of $\beta_\perp$ ($\beta_\|$), hence we ignore errors in $S_\|$ due to cross talk ($S_\| - S_\|^{\mathrm{meas}}$ is negligible compared to other uncertainties). We keep the two symbols for consistency until we drop all mention of $S_\|^{\mathrm{meas}}$ after discussing Figure 1.

We determine this instrumental constant, using atmospheric observations, as follows: data with a strictly linear correlation between minimum $S_\perp^{\mathrm{meas}}$ and $S_\|^{\mathrm{meas}}$ indicating the presence of liquid, not depolarizing particles only, plus the instrumental contribution to the perpendicular channel were sought. As an example, the $(S_\perp^{\mathrm{meas}}, S_\|^{\mathrm{meas}})$ dependence is shown in Figure 1 for 1 day in winter 1996/1997, an observation with a minimum $S_\|^{\mathrm{meas}}$, i.e., an almost purely liquid PSC. A linear least squares fit [see, e.g., *Press et al.*, 1986] of $S_\perp^{\mathrm{meas}}$ versus $S_\|^{\mathrm{meas}}$ (weighted with $1/\mathcal{E}(S_\perp^{\mathrm{meas}})^2$) yields a first-order instrumental constant δ^c. This constant is then used to calculate the preliminary, first-order corrected quantities $S_\perp$ and δ^{Aer} for all data of a winter. Now all those data points of a whole winter that are consistent with $S_\perp = 1$, $\delta^{\mathrm{Aer}} = 0$ (within error bounds) can be selected and the linear fit be applied to the selected raw data

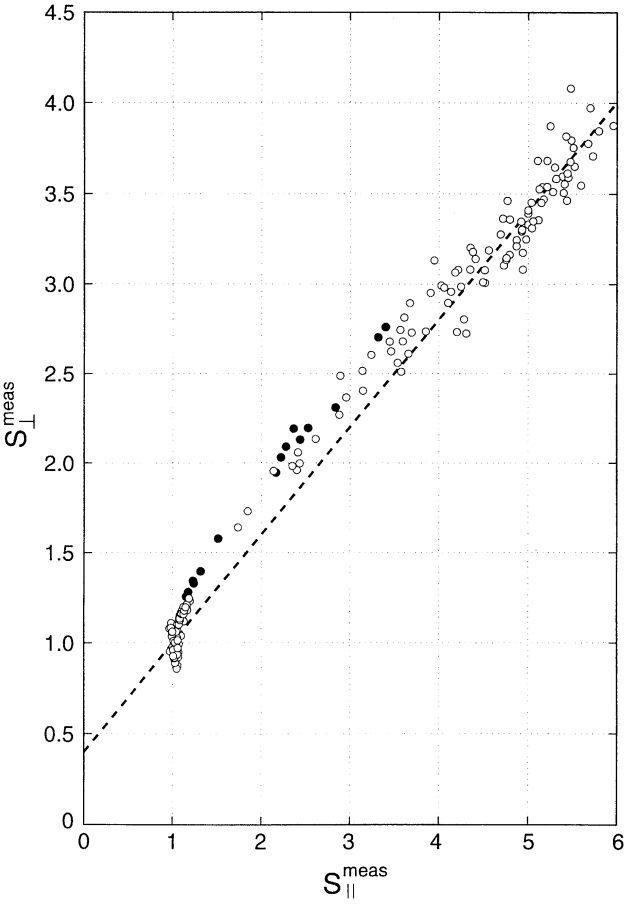

Figure 1. Quasi-linear correlation between measured parallel backscatter $S_\|^{\mathrm{meas}}$ and measured perpendicular backscatter $S_\perp^{\mathrm{meas}}$ on February 20, 1997, between 1834 and 2200 UT, in an almost purely liquid polar stratospheric cloud (PSC), illustrating the correction of instrumental cross talk between the parallel and perpendicular channels. Solid circles represent uncorrected raw data; open circles represent selected data after first correction step with aerosol depolarization $\delta^{\mathrm{Aer}} < 0.005$. Dashed line is weighted linear fit corresponding to $\delta^c = 0.0217$.

of a winter, yielding a second-order δ^c; the procedure is iterated once more and convergence checked.

It is found that the correction constant is $\delta^c \leq 0.0001$ for winter 1994/1995, $\delta^c = 0.0031 \pm 0.0005$ for winter 1995/1996 while $\delta^c = 0.0217 \pm 0.0020$ for winter 1996/1997. Especially in the winter 1996/1997 (with only one polarizing beam splitter employed), a significant correction was necessary.

While this procedure of correlating selected $S_\perp^{\text{meas}}$ with $S_\parallel$ corrects instrumental artifacts, it possibly overestimates the necessary instrumental correction, as it cannot be excluded that even the cases with the chosen minimum $S_\perp^{\text{meas}}$ (such as the liquid PSC in Figure 1) do contain some natural perpendicular aerosol signal. In any case, this procedure backs up the conclusions drawn below about solid particles in type Ib PSCs (and the occurrence frequency of mixed phase clouds could be even slightly higher).

2.5. Uncertainties

A standard deviation $\mathcal{E}$ of each variable (i.e., an absolute error) has been calculated for each observation. It includes random and systematic errors. The $\mathcal{E}$ obviously depends on the specific instrumental and atmospheric measurement conditions, thus it varies for each data point; however, for the bulk of data, an approximately fixed relative error in backscatter ratios can be given. For example, the relative uncertainty of the perpendicular backscatter ratio, denoted by $\mathcal{E}(S_\perp)/S_\perp$, has an average value of $\pm 18\%$. Other typical uncertainties include $\mathcal{E}(S_\parallel)/S_\parallel \approx \pm 10\%$ and $\mathcal{E}(S_t)/S_t \approx \pm 10\%$. Volume depolarization has an uncertainty $\mathcal{E}(\delta^{\text{Vol}}) \approx \pm 1\%$. The uncertainty of the aerosol depolarization, δ^{Aer}, depends strongly on total backscatter ratio; it can be expressed as $\mathcal{E}(\delta^{\text{Aer}}) \approx \pm 0.04/(S_t - 1)$. This is an empirical and approximate formula; of course, $\mathcal{E}(\delta^{\text{Aer}})$ depends also on the specific value of δ^{Aer} itself as well as on the specific measurement conditions; yet the dependence on S_t is dominant. A δ^{Aer} measurement at $S_t = 1.1$ has an uncertainty of typically $\pm 40\%$.

2.6. Resolutions

The original time resolution of the lidar data is $\sim$ 1 min; height resolution varies over different years and campaigns from 15 to 200 m. Here we present all data integrated uniformly to a height resolution of 200 m and a time resolution of 1 hour. The reason on the experimental side for such a rather coarse resolution in time and space is to ensure strong lidar returns, which may be normalized to the Rayleigh atmosphere at high altitudes without large statistical errors. This procedure covers also problematic cases; for example, deteriorated backscatter signals due to low tropospheric transmission.

The coarse resolution chosen here could lead to an apparent coexistence of solid and liquid particles, which would then be an artifact of the spatial and temporal averaging procedure. However, we observed simultaneous occurrence of liquid and solid particles on the smallest spatial and temporal scale resolvable by the lidar instrument (30 m, 1 min), as evidenced from both parallel and perpendidular backscatter ratio being significantly (2σ) above aerosol-free (molecular) backscatter. This cannot be the result of instrumental shortcomings (cross talk, etc.), as the fine structures of the $S_\perp$ and $S_\parallel$ profiles appear to be uncorrelated. Furthermore, tests with data evaluation using enhanced resolution (150 m and 10 min) show no significant difference in results without any indication of demixing. If the observed mixed clouds were composed of purely liquid and solid patches, these patches would always have to have horizontal dimensions smaller than typically 2 km, which appears to be very unlikely. In contrast, *Beyerle et al.* [2000] find typical spatial and temporal scales of PSC backscatter ratio and depolarization over Spitsbergen to be of the order of 1 km and 45–60 min, in accord with the present analysis.

2.7. Temperatures and Trace Gas Data

Accurate temperature profiles are crucial for the analysis of PSC observations. Here we use temperatures given by the local meteorological sondes, interpolated linearly to the time of the lidar observation. Instrumental errors are given by the manufacturer as ± 0.2 K, while we estimate errors produced by temporal interpolation and by spatial drift of the ballon as typically ± 1.3 K [*Biele*, 1999].

The equilibrium temperatures T_{NAT} and T_{ice} are calculated assuming realistic H_2O and HNO_3 profiles [*Biele*, 1999]. The adopted average water vapor profile has been constructed by averaging and smoothing recent measurements of H_2O in the Arctic vortex [Aellig *et al.*, 1996; *Schiller et al.*, 1996; *Ovarlez and Ovarlez*, 1994; *Vömel et al.*, 1997]; it rises from a minimum at 14 km altitude (3.9 ppmv) to 5.8 ppmv at 30 km. A time- and height-dependent profile is used for HNO_3; for this we use long-term Ny Ålesund Fourier transform infrared (FTIR) observations of the nitric acid column and the "degree-of-subsidence" parameter defined by *Notholt et al.* [1997] along with a model profile to calculate seasonal mean HNO_3 profiles peaking between 18 and 21 km (9.3 to 11.4 ppbv).

For the calculation of STS properties we need a sulfuric acid profile. As the remnants of the Mount Pinatubo sulfuric acid cloud have almost vanished in the years discussed here, we use a background H_2SO_4 profile given by *Warneck* [1988], peaking at 0.96 ppbv ($\sim$ 3 ppbm) in 18 km altitude. We assume a typical uncertainty of ± 1 ppmv in the water and ± 2 ppbv in the nitric acid content under not dehydrated or denitrified conditions. This leads to maximum additional errors of ± 1.3 K in both T_{ice} and T_{NAT}, leading to a maximum total uncertainty for the temperature differences $T - T_{\text{NAT}}$ or $T - T_{\text{ice}}$ of the order of ± 2.5 K.

Table 1. Definitions of Polar Stratospheric Cloud (PSC) Ia, Liquid Phase PSC Ib, and Mixed Phase PSC 1b[a]

PSC Type	Aligned Backscatter Ratio	Cross-Polarized Backscatter Ratio	Likely Physical Cloud Composition	Class
None	$S_\parallel < 1 + 2\,\mathcal{E}(S_\parallel)$[b]	$S_\perp < 1 + 2\,\mathcal{E}(S_\perp)$[b]	binary droplets	background aerosol only[c]
Ia, 26%	$S_\parallel < 1.2$	$S_\perp > 1 + 2\,\mathcal{E}(S_\perp)$	few[d] hydrate particles plus binary droplets	hydrate cloud
Ia-enh[e] 1%	$7 > S_\parallel > 1.5$	$S_\perp > 1 + 14(S_\parallel - 1)$[i]	some[g] hydrate particles plus little or no interstitials	hydrate cloud
Liquid phase Ib 50%	$S_\parallel > 1 + 2\,\mathcal{E}(S_\parallel)$	$S_\perp < 1 + 2\,\mathcal{E}(S_\perp)$	ternary droplets only	liquid cloud
Mixed phase Ib[f] 23 %	$7 > S_\parallel > 1 + 2\,\mathcal{E}(S_\parallel)$	$1 + 14(S_\parallel - 1) > S_\perp > 1 + 2\,\mathcal{E}(S_\perp)$[i]	ternary droplets plus hydrate particles	mixed phase cloud
II	$S_\parallel > 7$[h]	$S_\perp > 85$[h]	ice particles mixed with liquids/ solid hydrates	ice cloud

[a]Definitions are based on perpendicular backscatter $S_\perp$ and parallel backscatter $S_\parallel$ valid for Rayleigh depolarization $\delta^{\mathrm{Ray}} = 0.0144$.

[b]Criteria for $S_\parallel$ and $S_\perp$ depend on the absolute value of the standard deviations $\mathcal{E}$, which differ from data point to data point. Here backscattering ratios are assumed to be in the vicinity of 1, which yields the simplified formulas given here. In the above formulas, typically $\mathcal{E}(S_\parallel) \approx 0.10$ and $\mathcal{E}(S_\perp) \approx 0.18$.

[c]Note that the background aerosol (Junge layer) actually leads to a aligned backscatter ratio $S_\parallel > 1$, with a maximum of ~1.05 to 1.2, depending on the remnant volcanic load of the stratosphere.

[d]Typical nitric acid trihydrate (NAT) number densities are $10^{-4} \ldots 10^{-2}\mathrm{cm}^{-3}$.

[e]Note that Ia-enh here is identical with type Ic of *Toon et al.* [2000] and type Id of *Wedekind et al.* [1997]. See text.

[f]This is possibly identical to type M of *Rosen et al.* [1997].

[g]Typical NAT number densities are $> 10^{-1}\mathrm{cm}^{-3}$.

[h]Given values are only true when the ice number density is high (>0.5 cm^{-3}) and the ice particle radii are <3 μm.

[i]This corresponds to a minimum aerosol depolarization $\delta^{\mathrm{Aer}} = 0.2$ of the solids present; $14 = 0.2/0.0144$. Rescale for lidar systems with other values of the Rayleigh depolarization.

3. Observations

According to meteorological data analysis of eight winters (1989/1990 to 1996/1997) by *Stebel* [1998], the multiwavelength lidar in Ny Ålesund on Spitsbergen (79°N, 12°E) lies in the center of the Arctic vortex most of the time. An average of 25% of all measurement days show PSCs and this increases to as much as ≈63% for the cold winters 1995/1996 and 1996/1997. The PSCs above Ny Ålesund are not affected by local orographic effects as, for example, are PSCs in the vicinity of the Scandinavian mountain ridge. The Ny Ålesund observations are therefore more representative of the relatively slowly varying synoptic conditions of the Arctic vortex center.

3.1. Data Overview

In the time period between January 11, 1995, and March 6, 1997, we assembled altogether 525 hourly vertical lidar profiles of which 421 showed PSC signatures (see Table 1 for the definition of PSC existence). They have been combined to form a large database of ~20,000 data points, each data point representing the optical and meteorological data integrated over 1 hour and 200 m. As stratospheric temperatures above Ny Ålesund only rarely drop below the frost point (T_{ice}), type II PSCs have never been identified unambiguously in this data set.

Figure 2 shows the relative abundances of type Ia and type Ib PSCs over Ny Ålesund during the three winters on a joint time axis. The data have been binned into 3.5 days time bins. About 26% of all observations fall into the traditional type Ia set, ~73% fall into the traditional type Ib set, and the remaining 1% are type 1a-enh PSCs (not shown). Type Ib PSCs are further divided into subclasses "purely liquid" for PSCs with $S_\perp < 1.36$ within instrumental uncertainty and "mixed" with $S_\perp > 1.36$, i.e., with clear indication of the presence of solid particles inside these predominantly liquid clouds, most likely liquid/solid external mixtures. Here $S_\perp = 1 + 2 \times \mathcal{E}(S_\perp) = 1.36$ reflects two standard deviations of the perpendicular backscatter ratio in the Ny Ålesund data set, while "any PSC" is defined as either $S_\perp$ or $S_\parallel$ or both significantly, 2 errorbars, greater than unity. Thus the precise occurrence frequencies of purely liquid type Ib clouds and type Ib clouds with solid particles (50% and 23%, respectively) are subject to instrumental precision. However, with the arguments on instrumental artifacts (cross talk, etc.) and spatial/temporal resolution and averaging given above, we expect the numbers given in Figure 2 to be a reasonable representation of the actual PSC prop-

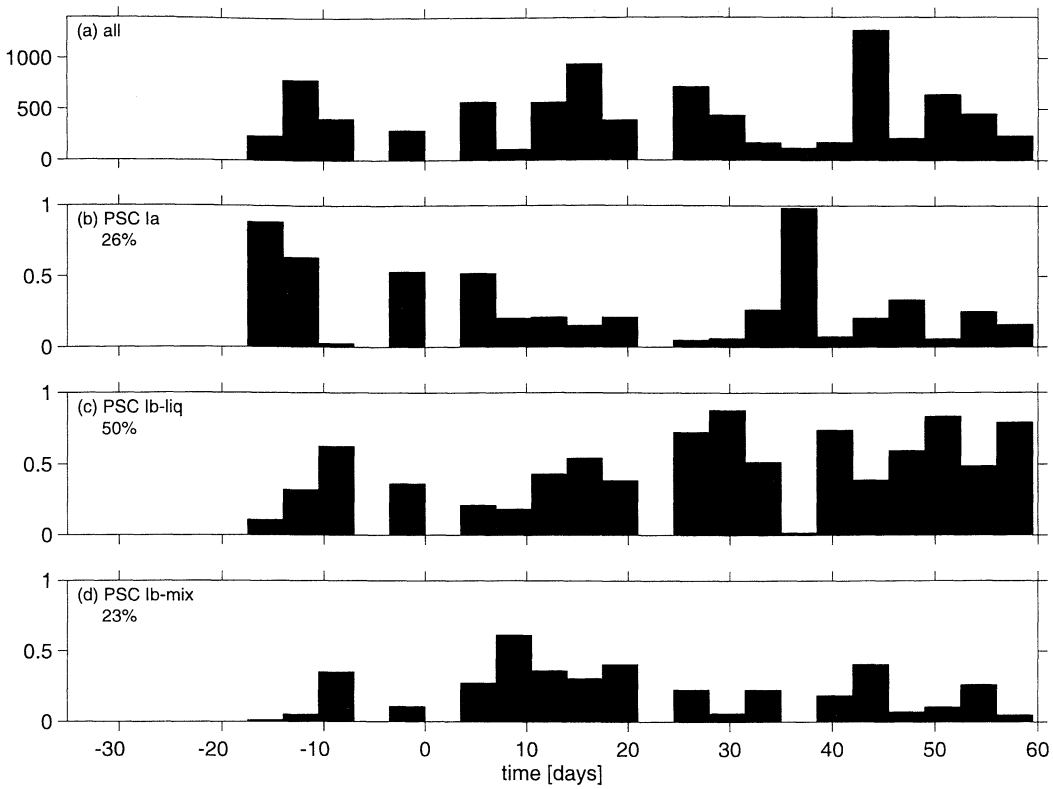

Figure 2. Combined statistics of lidar observations at Ny Ålesund in the winters 1995–1997 (time=0 corresponds to January 1). (a) PSC occurrence observations (all types) with data binned in 3.5 day intervals. Time bins with <100 observations have been discarded. Also shown are the occurrence frequencies of (b) PSC Ia (26% of all PSC observations), (c) purely liquid phase PSC Ib (50% of all PSC observations), and (d) mixed phase PSC Ib (23% of all PSC observations) normalized by the total number of observations. Cloud classification is according to Table 1.

erties over Ny Ålesund. From Figure 2 it is further clear that there is no obvious trend of the various types of PSCs throughout these winters.

An inspection of all individual profiles revealed that most of them contain solid particles at some altitude. While PSCs that contain mostly liquid particles show minimum temperatures of at least 4 K below T_{NAT}, clouds without a purely liquid fraction show minimum temperatures only marginally below T_{NAT}.

This behavior is consistent with cold PSCs ($\sim$ 4 K below T_{NAT}) containing mostly STS particles and warm PSCs (just below T_{NAT}) containing NAT particles but no STS droplets. Compared to NAT other nitric acid hydrates, e.g., the dihydrate (NAD), appears to be a less likely explanation of the observed depolarization signals because the NAD existence temperatures are at least 2 K below that of NAT, although the existence of NAD cannot be excluded.

3.2. Polarization Versus Backscatter Ratio

Plate 1 shows the 532-nm backscatter signals plotted in the traditional form as aerosol depolarization (δ^{Aer}) versus total backscatter ratio (S_t). It is seen that most of the $S_t/\delta^{\mathrm{Aer}}$ space is empty, as almost all of the data cluster either at the depolarization axis or at the backscatter ratio axis, corresponding to PSCs of type Ia and type Ib, respectively. Many points also cluster near the origin, corresponding to background aerosols (small H_2SO_4/H_2O droplets with little uptake of HNO_3).

Plate 1 shows the measurements in the time interval stated above excluding three nights (December 21/22, 1995; January 6, 1996 and February 6, 1996) on which the observed S_t and δ^{Aer} values deviated considerably from the general Ia/Ib behavior. These observations, which correspond to $\sim$1% of all data points, show characteristics of type Ia-enh PSCs and are discussed in detail by *Tsias et al.* [1999]. Data points belonging to this rare kind of clouds have been eliminated from the present analysis (affecting $\sim$1% of all measurements).

In Plate 1, temperature, expressed as $T - T_{\mathrm{NAT}}$, is given by a color code. Observations showing high depolarization generally belong to higher temperatures than observations showing large backscatter ratio. More precisely, type Ia clouds are seen mostly at 0–4 K below T_{NAT}, while type Ib clouds correspond mostly to even lower temperatures ($T \leq T_{\mathrm{NAT}} - 4$ K). Assuming type Ia clouds to contain NAT particles and type Ib clouds to consist of ternary droplets, the temperature attribution

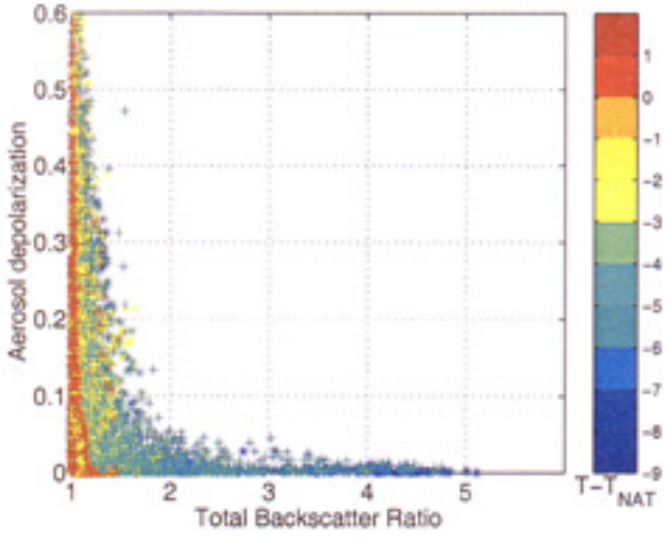

Plate 1. Scatterplot of aerosol depolarization $\delta^{\mathrm{Aer}} = \beta_{\perp}/\beta_{\parallel}$ versus total backscatter ratio S_t. Data points cover 99% of all observations 1995–1997; the remaining 1% of type 1a-enh polar stratospheric clouds (PSCs) scatter over the entire (S_t,δ^{Aer}) plane and are suppressed for clarity. Color coding is according to the temperature difference $T - T_{\mathrm{NAT}}$. Data from January 1995 subject to denitrification are plotted as stars, all others as crosses. Most data points are found either near the depolarization axis ("Ia") or near the backscatter ratio axis ("Ib"), while background aerosol measurements are near the origin. Uncertainties are $<\sim$10% for S_t and $\sim 0.04/(S_t - 1)$ for δ^{Aer}.

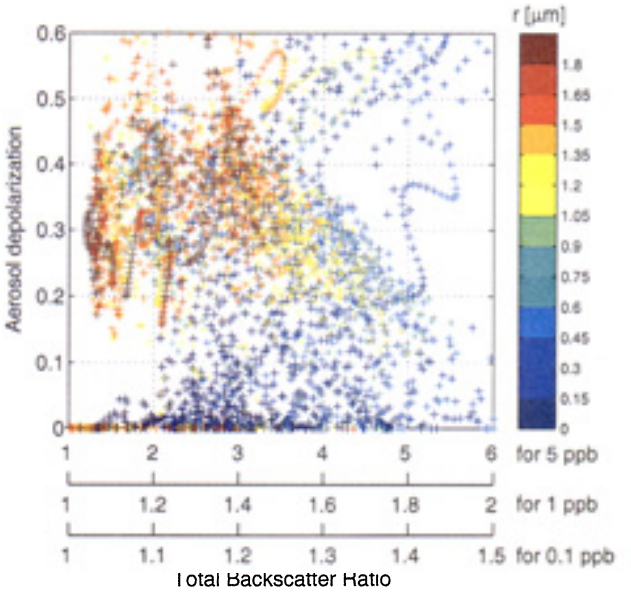

Plate 2a. Theoretical T matrix calculations of aerosol depolarization $\delta^{\mathrm{Aer}} = \beta_{\perp}^{\mathrm{Aer}}/\beta_{\parallel}^{\mathrm{Aer}}$ versus total backscatter ratio. Backscatter/depolarization properties are simulated for a PSC consisting only of NAT particles corresponding to 5 ppbv condensed HNO_3. Particles are monodisperse but occur with varying aspect ratios between 0.5 and 1.5 and various radii (color code). Amounts of condensed HNO_3 other than 5 ppbv lead to a rescaling of the abscissa (see axes for 1 and 0.1 ppbv). Number density, radius and condensed HNO_3 of NAT particles are 0.005 cm^{-3}, 1.56 μm, and 0.335 ppbv, respectively, while their aspect ratios vary, $\epsilon = 0.5 \ldots 1.5$.

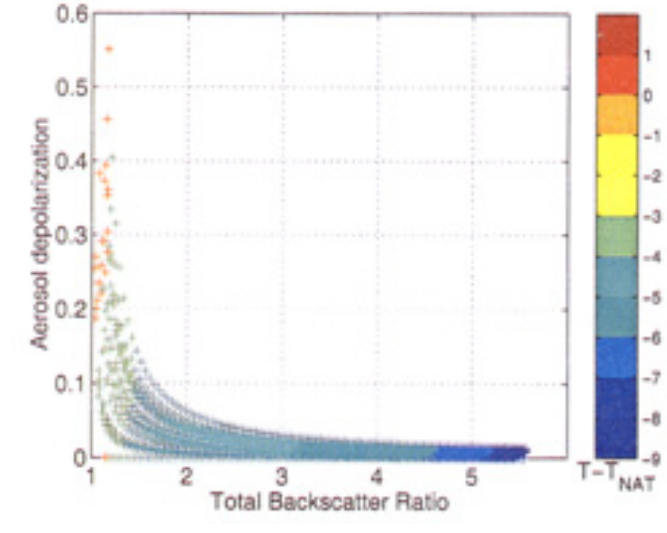

Plate 2b. Theoretical T matrix calculations of aerosol depolarization $\delta^{\mathrm{Aer}} = \beta_{\perp}^{\mathrm{Aer}}/\beta_{\parallel}^{\mathrm{Aer}}$ versus total backscatter ratio of a mixed cloud. Calculation assuming a fixed NAT distribution but varying STS abundance. Number density, radius and condensed HNO_3 of NAT particles are 0.005 cm^{-3}, 1.56 μm, and 0.335 ppbv, respectively, while their aspect ratios vary, $\epsilon = 0.5 \ldots 1.5$ (as in Plate 2a). STS particle distribution (distribution width $\sigma = 1.8$ and fixed number density of 10 cm^{-3}) with condensed HNO_3 amount varies from 0 to 10 ppbv depending on temperature (same color code for $T - T_{\mathrm{NAT}}$ as in Plate 1).

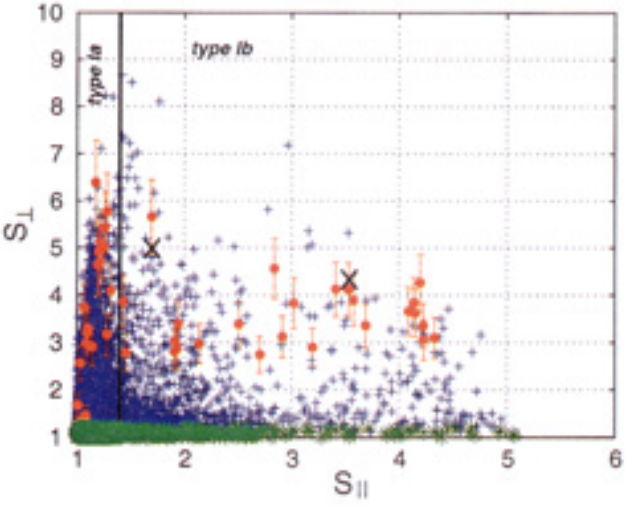

Plate 3. Scatterplot of perpendicular backscatter ratio $S_{\perp}$ versus parallel backscatter ratio $S_{\parallel}$. Solid vertical line at $S_{\parallel} = 1.4$ marks maximum backscatter ratio for type Ia PSCs after *Browell et al.* [1990]. Red circles with error bars indicate data points taken from the lidar profile shown in Figure 6. Green stars at the bottom are measurements that show a perpendicular backscatter ratio consistent with 1.0, i.e., purely liquid type Ib clouds.

given in Plate 1 is in accordance with what is expected from equilibrium thermodynamics, as T_{STS} is 3 to 4 K below T_{NAT}. Note, however, that measurements with high S_t but low aerosol depolarization may still contain a minority of solid particles whose depolarization signal is "masked" by the high parallel backscatter ratio of the liquid aerosol.

3.3. Temperature Dependence

We tried to avoid misrepresentation of temperatures by a critical analysis of the Ny Ålesund sonde data. Owing to large temperature uncertainties or errors in some meteorological sondes the following observation days have been discarded from all plots relying on temperature information: December 23, 1995; January 17/18, 1996; January 21, 1996; February 4, 1996; and February 20–22, 1997. Furthermore, it should be noted that in this and the following plots, PSC data from January 1995 show a bias toward lower temperatures. As will be discussed below, this is probably a result of denitrification, which was strong in that winter [*Waibel et al.*, 1999]. These points are plotted as asterisks instead of crosses to distinguish them from the other data. Typically, all points belonging to the lowest temperatures $T - T_{NAT} < -7$ K fall into this category (which amounts to 11.2% of the entire data set).

In Figure 3 we present all profiles in a scatterplot of the cloud fraction containing solid particles, $\mathcal{F}_{solid}$ versus $\min(T - T_{NAT})$. Each point corresponds to one of the 421 lidar profiles containing PSCs plotted over the minimum temperature within the cloud with respect to T_{NAT}. The dotted vertical line indicates T_{STS}. At $T \gtrsim T_{STS} + 0.8$ K, most profiles (except a few outliers) contain solid particles at all altitudes, as only hydrate particles (together with interstitial binary H_2SO_4/H_2O droplets) can exist in this temperature range ($T_{NAT} \approx T_{STS} + 3.6$ K and $T_{NAD} \approx T_{STS} + 1.6$ K). This is to be expected, as liquid aerosols at these temperatures do not take up appreciable amounts of HNO_3 and therefore are too small to contribute significantly to the parallel backscatter signal. Below T_{STS} there are apparently random values of $\mathcal{F}_{solid}$ between 0 (only liquid particles in the entire profile) and 1 (solid particles are present everywhere). This suggests that the presence of solid, most likely NAT particles in PSCs below T_{STS}, is independent of the temperature at the time of the observation, but it may depend on other factors, such as the (temperature) history of the particular air parcels forming the cloud.

Figure 4 shows the parallel backscatter ratio $S_{\|}$ (of solid plus liquid particles) versus $T - T_{NAT}$ along with theoretical growth curves for STS and NAT. While backscatter ratios at $T > T_{NAT}$ are temperature independent, they increase at and below the STS dew point (bold dashed vertical line). Gray solid curves indicate theoretical simulations of the backscatter ratio by STS droplets under equilibrium conditions (calculated by means of the coupled STS thermodynamic and optical, i.e., Mie scattering, models described by *Carslaw et al.* [1998]). The individual STS curves actually broaden into bands with typical width ±0.7 K to account for nonequilibrium effects due to mesoscale temperature fluctuations as shown by *Bacmeister et al.*

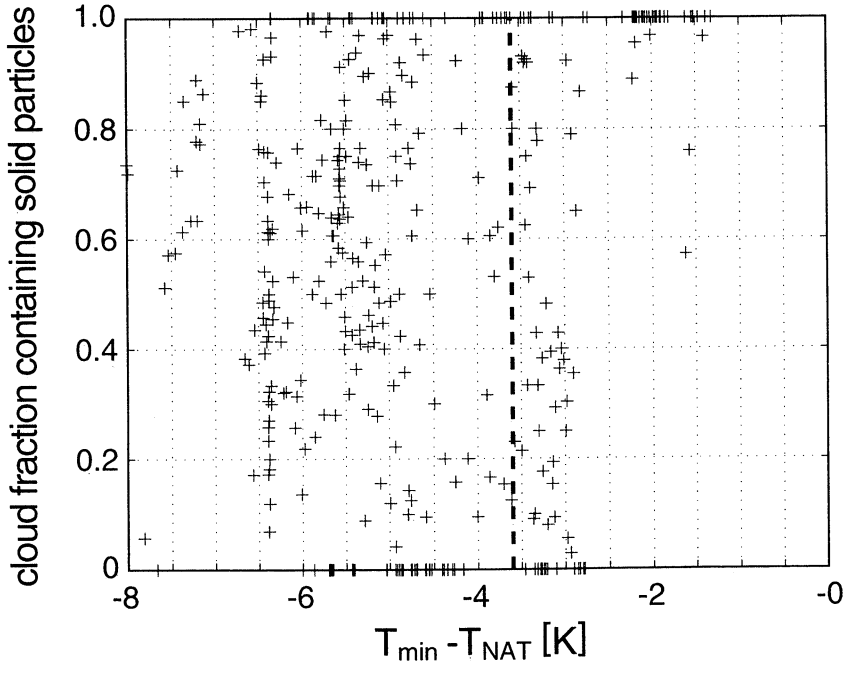

Figure 3. Fraction of individual cloud profiles containing solid particles, $\mathcal{F}_{solid}$, plotted versus $\min(T - T_{NAT})$, i.e., the lowest temperature within the cloud profile relative to T_{NAT}. Dashed vertical line indicates T_{STS}. $\mathcal{F}_{solid}$ is defined as the number of altitude bins in a PSC profile where solid particles could be detected, divided by the total number of height bins containing any PSC.

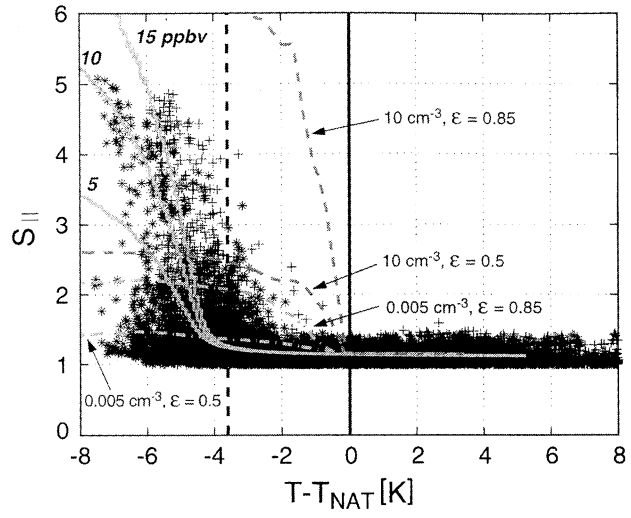

Figure 4. Scatterplot of parallel backscatter ratios ($S_{\|}$) versus $T - T_{\mathrm{NAT}}$. Typical experimental uncertainties are ±15% for $S_{\|}$ and ±2.5 K for $T - T_{\mathrm{NAT}}$. Dashed and solid vertical lines indicate T_{STS} and T_{NAT}, respectively. For comparison, lines show calculated backscatter ratios for a H_2O content of 5 ppmv: Solid curves are Mie calculations of supercooled ternary solution (STS) backscatter ratios for equilibrium conditions with various HNO_3 concentrations (parameters on the curves, in ppbv). Dashed curves show T matrix computations for NAT particle equilibrium sizes with number densities of 0.005 cm^{-3} (dash-dotted line) and 10 cm^{-3} (dashed line) and two aspect ratios (0.5 and 0.85, indicated on the curves).

[1999]. Given this and the experimental temperature error bar of ±2.5 K, we find reasonable consistency with the STS model. Data of January 1995 are again marked with different symbols (stars instead of crosses), as they exhibit a systematic bias toward lower temperatures. Some points show only moderate $S_{\|}$ (< 2.5), even at very low T (< T_{NAT} − 6 K), which may be partly explained in terms of denitrification [*Waibel et al.*, 1999]. Denitrification was found to lower HNO_3 around 20 km by up to a factor of 2, and consequently, T_{NAT} temperatures are lowered by ≃1 K in comparison to those calculated with our standard profiles. Finally, the dashed and dotted curves in Figure 4 are simulations for NAT particles, which will be discussed in section 4.

Figures 5a and 5b show the volume depolarization δ^{Vol} versus $T - T_{\mathrm{NAT}}$, comprising the measurements during the three winters 1994–1997 at all altitudes. Volume depolarization is used rather than aerosol depolarization since δ^{Vol} is "well behaved" in terms of uncertainties in contrast to δ^{Aer}. The Rayleigh value $\delta^{\mathrm{Vol}} = 0.0144$ of aerosol-free air (referring to the detector bandwidth in our measurements) is marked by the horizontal dashed line to guide the eye. It is seen that while at $T > T_{\mathrm{NAT}} + 2$ K the measurements are centered on the value of Rayleigh depolarization for aerosol-free air, measurements below that temperature show depolarization increasing to 5 times the Rayleigh value and some even higher. Below $T_{\mathrm{NAT}} - 3$ K, further events with volume depolarization lower than the Rayleigh value occur. Values $\delta^{\mathrm{Vol}} > 0.0144$ indicate that the depolarization due to solid aerosols exceeds any effect of liquid aerosols. Conversely, $\delta^{\mathrm{Vol}} < 0.0144$ is a signature of mostly liquid (i.e., spherical) particles in the volume probed, which lead to a lower depolarization than that of molecular air. The onset of highly depolarizing PSC particles is consistent with the NAT condensation temperature, T_{NAT}, taking into account that the quantity $T - T_{\mathrm{NAT}}$ has an uncertainty of ±2.5 K. Similarly, observations below the Rayleigh value are consistent with the STS formation temperature, $T = T_{\mathrm{NAT}} - 3.6$. Note

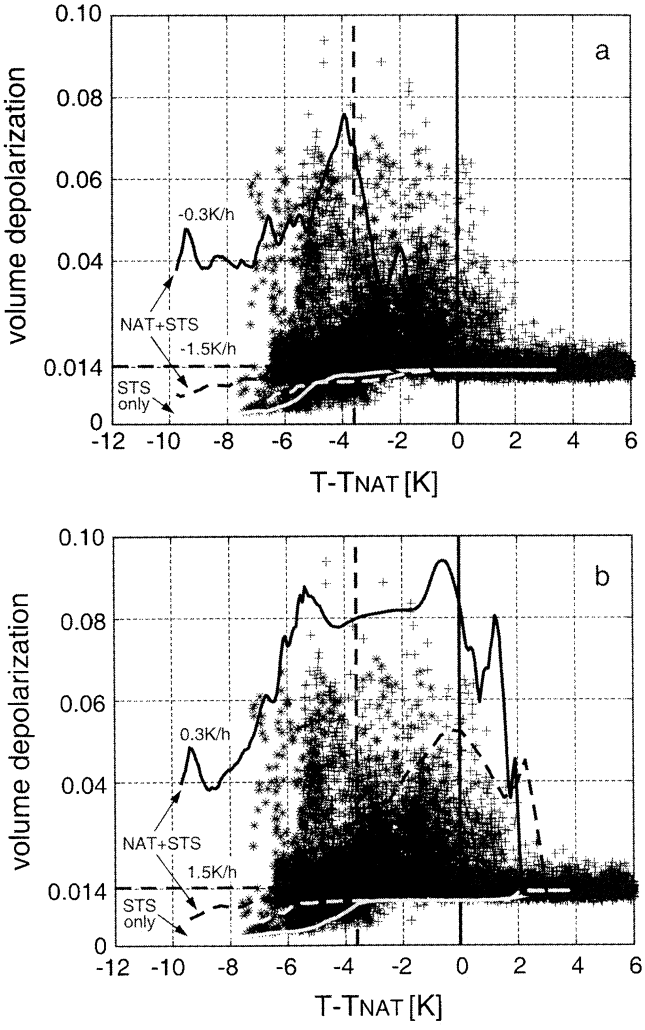

Figure 5. Scatterplot of volume depolarization data $\delta^{\mathrm{Vol}} = \beta_{\perp}/\beta_{\|}$ versus $T - T_{\mathrm{NAT}}$ (data of January 1995 shown as stars, all others as crosses). The Rayleigh depolarization of 1.44% is indicated by a dashed horizontal line. Theoretical curves are given for pure STS (lower light curves)and two different mixtures of NAT particles with STS droplets. (a) Theoretical curves computed for a constant cooling rate of 1.5 (0.3) K/h for the last 10 (50) hours (dash-dotted, solid lines, solid for the STS curve) and for an aspect ratio $\epsilon = 0.85$. (b) Results for the subsequent heating period with the same parameters, STS curve dashed (also see text).

that the quantity $\delta^{\mathrm{Vol}} = \beta_\perp/\beta_\parallel$ may be lowered by populations of large STS droplets, if the number densities and sizes of the solid particles are not too high. This will occur as the temperature falls and STS droplets grow, even if $\beta_\perp$ remains constant or is slowly increasing. The curves in Figures 5a and 5b are simulations of optical properties of mixed (solid/liquid) PSCs, which will be explained in section 4.

4. Theoretical Calculations

We simulate the observations shown above with microphysical and optical models based on certain assumptions concerning ensembles of liquid and solid particles. All calculations have been performed for the 50-hPa pressure level, equivalent to an altitude of ~20 km. However, the results are almost invariant with pressure when plotted against $T-T_{\mathrm{NAT}}$, so they can be compared directly to our lidar data for a wide altitude range. The transformation of the temperature axis from T to $T - T_{\mathrm{NAT}}$ is effective because $T_{\mathrm{STS}} - T_{\mathrm{NAT}}$ is approximately independent of HNO_3 and H_2O partial pressures and hence modest changes in total pressure.

By means of a light-scattering algorithm it is possible to convert assumed, observed, or calculated particle size distributions into a simulated lidar signal. By comparing the results of the optical simulation with the observed lidar signal, certain parameters for the particle distributions can be constrained. Light scattering is easily calculated for spherical particles using Mie theory. For nonspherical particles, which are of central interest here, we applied the T matrix method [*Mishchenko*, 1991], assuming the particles to be of spheroidal shape. We have shown this simplifying assumption to work successfully in our previous PSC studies [e.g. *Carslaw et al.*, 1998].

4.1. Polarization Versus Backscatter Ratio

First, we turn to the simulation of the experimental data shown in Plate 1. We start out with the most simple assumption of a NAT PSC in equilibrium with the gas phase typical for an Arctic lower stratospheric air parcel. We assume that 5 ppbv of HNO_3 have been condensed onto the NAT particles (i.e., about half of the total HNO_3 available in such an air parcel). As we have no information on number densities or asphericities of NAT particles, we applied the T matrix calculations to monodisperse NAT size distributions with widely varying radii ranging from 0.1 to 2.0 μm and 21 different aspect ratios $\epsilon = 0.5 \ldots 1.5$ for each radius. Because the amount of condensed nitric acid is fixed (5 ppbv) while radii vary, the number density of NAT particles varies accordingly (small radii leading to high number densities and vice versa). The result of this calculation is shown in Plate 2a with the color code indicating particle radius.

It is evident that with 5 ppbv HNO_3 in the condensed phase, most of the $\delta^{\mathrm{Aer}}/S_t$ space is filled, in striking contrast to the type Ia/Ib PSC scheme displayed in Plate 1. This situation is not changed if only single radii or asphericities are chosen. With radii >2 μm, more points are added with low backscatter ratio at all depolarizations, although backscatter ratios remain too high to match observations. Also, the result is practically independent of the assumption that the particles are monodisperse, as other calculations for lognormal distributions show (not shown here).

The only way to obtain smaller backscattering ratios at moderate to high depolarization ratios, as shown by the observations, is to reduce the amount of nitric acid condensed in the solid particles. This leads simply to a different scaling of the abscissa, i.e., the total backscatter ratio axis (see Plate 2a, lower two abscissas). Typical $\delta^{\mathrm{Aer}}/S_t$ values for type Ia PSCs are approached for 1 to 0.1 ppbv HNO_3 in the condensed phase. This is a surprising finding at first sight, as, at most, 5% of the total available HNO_3 is allowed to condense.

A more realistic simulation requires taking both solid and liquid particles into account, as predominantly liquid particles are responsible for type Ib properties and predominantly solid particles for type Ia properties. According to the scaling of backscatter ratio with condensed solid mass shown in Plate 2a, condensed solid mass has to always remain <1 ppbv of HNO_3. On the other hand, condensed liquid mass has to occur in varying amounts to account for type Ib backscatter ratio varying between 1.5 and 6 (abscissa). Plate 2b shows such a T matrix calculation with a mixed particle distribution of STS and NAT particles. In this example we use a narrow lognormal size distribution for the NAT particles with mean radius $R_{\mathrm{mod}} = 1.56$ μm, distribution width $\sigma = 1.01$, and the constraint that 0.335 ppbv HNO_3 be condensed onto NAT particles with a number density of 0.005 cm^{-3}. Again, 21 different aspect ratios $\epsilon = 0.5 \ldots 1.5$ have been used for the computations and are all shown in Plate 2b. For the STS size distribution we assume typical values: $\sigma = 1.8$ and a fixed number density of 10 cm^{-3}. The amount of HNO_3 condensed into STS droplets varies from 0 to 10 ppbv, depending on temperature. The STS droplets are assumed to be in equilibrium with the gas phase, with vapor pressures calculated according to *Carslaw et al.* [1994]. Temperature is shown as $T - T_{\mathrm{NAT}}$, and the same color code is used as in Plate 1. It is seen that at temperatures near T_{NAT} (orange and red), the NAT particles dominate the backscatter characteristics of the mixed cloud with high δ^{Aer} and low S_t, resembling values typical for type Ia PSCs. Lowering the temperature leads to uptake of nitric acid by the liquid aerosol and thus to higher S_t but lower δ^{Aer}. At the lowest temperatures, highest backscatter ratios are obtained while the aerosol depolarization has almost fallen to 0 (typical for type Ib PSCs).

We would like to emphasize that the restriction of solid phase HNO_3 to below 5% of the total available HNO_3 is the only possibility to achieve agreement between the observations and the T matrix model used

in the present study (compare measurements with high δ^{Aer} in Plate 1 with abscissas of calculations in Plate 2a). In principle, there might be other ways of simulating the observations, if the constraint of spheroidal particles is relaxed. However, test calculations using the T matrix model for rectangular cylinders instead of spheroids with radii and aspect ratios similar to those used above show no principally different result. Also, as mentioned above, previous detailed case studies allowed excellent descriptions of particle growth based on the present spheroid model [*Carslaw et al.*, 1998; *Tsias et al.*, 1999, and references therein].

Furthermore, it should be noted that the fixed amount of HNO_3 condensed as NAT (here 0.335 ppbv in 0.005 cm^{-3} particles with $R_{\mathrm{mod}} = 1.56\,\mu m$) leads to a small, but nonvanishing aerosol depolarization even at high backscatter ratios when liquid particles have taken up most of the available HNO_3. The agreement between the model calculations in Plate 2b and the observations in Plate 1 suggests that the observations can be explained by PSCs containing a small number of relatively large solid particles (e.g., NAT) externally mixed with a large number (10 cm^{-3}) of relatively small (0.1 to 0.3 μm) liquid particles (e.g., STS).

4.2. Temperature Dependence

The curves in Figures. 4 and 5 have been calculated with our microphysical model originally developed by *Meilinger et al.* [1995] to describe the growth kinetics of liquid particles and later generalized by *Tsias et al.* [1997] for solid particle nucleation. The model treats growth kinetics of liquid and solid aerosols by means of a Lagrangian scheme for aerosol radii, which enables one to accurately follow the evolution of nonequilibrium particle distributions.

In Figure 4 we follow air masses that cool very slowly so that the particles are in quasi-equilibrium and model $S_{\|}$ due to STS and NAT. Solid lines represent the parallel backscatter ratio of pure STS aerosol calculated for different concentrations of HNO_3 varying from 5 to 15 ppmv. As expected, the backscatter ratio is seen to increase strongly due to increasing uptake of nitric acid and water below T_{STS} (indicated by a dashed vertical line). Despite the relatively large uncertainties in temperature, many of the $S_{\|}$ observations during the three winters in Ny Ålesund are in satisfactory agreement with the modeled STS clouds, which dominate the parallel backscatter properties, but cannot explain the depolarization observed in many PSC events. Modeled $S_{\|}$ for NAT particles embedded in a background aerosol distribution under equilibrium conditions is shown by the dashed [$n(\mathrm{NAT}) = 10$ cm^{-3}] and dash-dotted [$n(\mathrm{NAT}) = 0.005$ cm^{-3}] lines for two aspect ratios ($\epsilon = 0.5$ and 0.85). Clearly, none of these curves is a good overall description of the observed $S_{\|}$, again suggesting that NAT in equilibrium with the gas phase is unlikely to be present in any of PSCs observed, irrespective of the particle number density or asphericity. An exception might be the observations of January 1995 (marked by stars instead of crosses), which show very low $S_{\|}$ at low temperatures that are best explained in terms of strong denitrification and the existence of very large NAT particles [*Waibel et al.*, 1999].

The microphysical calculations shown by the curves in Figures 5 assume a cooling (Figure 5a) and a heating (Figure 5b) air parcel with total mixing ratio of 5 ppmv H_2O and 10 ppbv HNO_3. Initially, under warm conditions with no HNO_3 taken up by the aerosol, the air parcel is assumed to contain a lognormal liquid particle distribution with total number density 10 cm^{-3}, mode radius $R_{\mathrm{mod}} = 0.08\,\mu m$, and lognormal width $\sigma = 1.8$, as is characteristic for the Arctic lower stratospheric aerosol. Light curves below the Rayleigh depolarization (1.44%) show the volume depolarization ratio of air containing only spherical STS droplets, while dark curves above the Rayleigh depolarization show 0.005 cm^{-3} of crystalline NAT particles with aspect ratio $\epsilon = 0.85$ externally mixed into the STS droplets. For both cases, two cooling rates are distinguished in Figure 5a by dashed (1.5 K/h) and solid (0.3 K/h) curves. Calculated maxima of depolarization occur around T_{STS}, while δ^{Vol} decreases again for still lower temperatures owing to increased parallel backscatter ratio of the liquid particles. Smaller cooling rates lead to more uptake of nitric acid by the NAT particles, so that the resulting depolarization is higher than for a faster cooling.

Figure 5b shows the calculated depolarizations under the same assumptions as in Figure 5a, but for a warming air parcel after it had reached a minimum temperature of $T - T_{\mathrm{NAT}} = -10$ K. Depolarizations are seen to rise to their maximum at higher temperatures than in the cooling phase and exhibit high values even for temperatures a few kelvins above T_{NAT} or up to 6 hours after T_{NAT} was passed. This is caused by the slowing of the evaporation/growth process of large NAT particles due to gas phase impedance (and, to a smaller degree, also surface accommodation impedance).

For other aspect ratios in the range $0.5 \leq \epsilon \leq 1.5$ the curves are qualitatively similar but have lower depolarizations; that is, the curves shown here represent an upper bound for the given ϵ range and the two specified cooling rates. Higher depolarizations may be reached when cooling/warming rates are even smaller. However, the NAT particles then grow to radii above 3.0 μm, which is the limit of applicability of the T matrix code used in the present calculations.

The calculated depolarization curves in Figures 5a and Figure 5b cover practically the entire range of observational data. The difference in the simulated growth and evaporation sequences suggests that the depolarization signal is strongly influenced by kinetic effects (mainly due to gas phase diffusion impedance), leading to NAT particle distributions that are not in equilibrium with the gas phase. In contrast, the backscatter curves (Figure 4), which are dominated by STS aerosols, are much less dependent on kinetic growth effects

because equilibrium is rapidly established between the gas phase and the large number of droplets. (Nonequilibrium effects among small and large droplets as they have been described by *Meilinger et al.* [1995] lead to only moderate changes in the backscatter ratio.)

5. Coexistence of Solid and Liquid Aerosols

As discussed above, the T matrix simulations can explain the observed δ^{Aer} versus S_t characteristics of the Ny Ålesund lidar data if solid and liquid particles are allowed to coexist and to develop kinetically (taking account of gas phase diffusion and surface accommodation effects). In the following we look at one specific observation and then generalize this case.

5.1. Case Study

A typical example of a mixed cloud is shown in Figure 6. Figure 6a shows $S_\perp$ and $S_\parallel$ and Figure 6b shows the volume and aerosol depolarizations of a PSC on February 12, 1997. This PSC looks like a typical "sandwich PSC" if only depolarization and parallel (or total) backscatter ratio are regarded, but the profile of $S_\perp$ indicates the continuous presence of solid particles in the central STS layer. Edges with high depolarization around type Ib PSCs were first recognized by *Poole and McCormick* [1988] and later by *Toon et al.* [1990], when the existence of STS droplets was not yet established. These authors argued that the supercooling remained low at the cloud edges, so that frozen HNO_3 hydrate

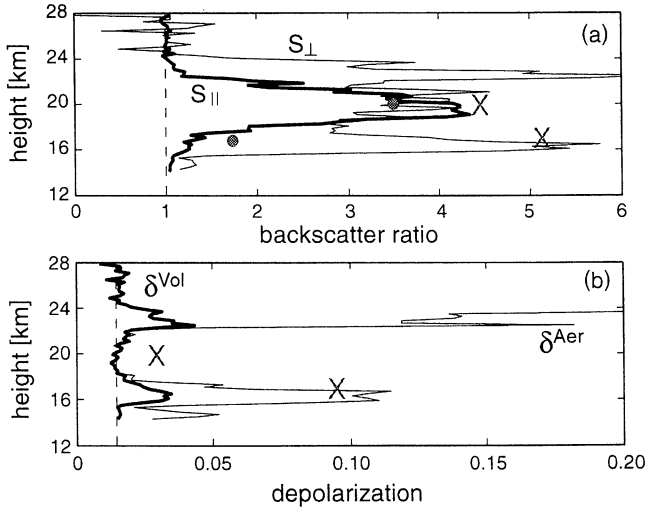

Figure 6. Example of a mixed PSC on February 12, 1997 (0500–0600 UT). (a) Vertical profiles of parallel (thick line) and perpendicular (thin line) backscatter ratios. (b) Corresponding profiles of volume depolarization (thick line) and aerosol depolarization (thin line). Vertical dashed lines indicate aerosol-free atmosphere ($S_t = 1$ and $\delta^{\mathrm{Vol}} = 0.0144$). Large superimposed dots and crosses show the end values of the theoretical simulation; see Figure 7. In Figure 6a, dots refer to $S_\parallel$ and crosses to $S_\perp$, while Figure 6b, the crosses refer to δ^{Aer}.

particles (like NAT) could grow to large sizes and consequently high depolarization, whereas the cloud core supercooled substantially and sufficiently rapidly to cause a large fraction of particles to freeze, resulting in many small particles with low depolarization. Today it is clear that the main properties of the cloud core are best explained in terms of STS droplets. In contrast to the assumption underlying the original explanation by *Toon et al.* [1990], nitric acid hydrates do not easily form in ternary solution droplets [e.g., *Koop et al.*, 1995].

Such PSCs with type Ib cloud core and type Ia solid particle layers at base and top have been termed "sandwich clouds" by *Shibata et al.* [1997] and *Biele et al.* [1997a, b], but these authors did not address the problem as to why there should be solid particles at the cloud edges but none in the cloud core. *Shibata et al.* [1999a, b] shed light on this question by showing that it could be possible that also the cloud center could contain a minority of solid particles. The present analysis shows clearly that solid aerosol particles do exist over the full altitude range (wherever $T < T_{\mathrm{NAT}}$), coexisting with the binary or ternary droplets. In contrast to the depolarization ratio, $S_\perp$ is not "masked" by high parallel backscatter. The solid particles give rise to cloud properties characteristic of type Ia. Thus, as suggested by Plates 2a, 2b, they assume only small particle number densities which do not have enough time to develop their equilibrium size, that is, they absorb only a small fraction of the available HNO_3 and yield small backscatter ratio and moderate depolarization. In contrast, the cold center layer of the cloud in Figure 6 allows temperatures to drop below T_{STS}, so that the majority of liquid particles have no difficulties in readily growing into well-developed STS droplets. These show a considerable backscatter ratio in the parallel channel, while the perpendicular backscatter ratio is maintained by the few solid particles in this external mixture.

As noted above (see section 2.4) cross talk is unlikely to be the reason for this observation. Rather, the cross talk correction may have led to a slight underestimation of $S_\perp$ inside the liquid cloud. However, the structure of the cloud in Figure 6 where maxima of $S_\parallel$ and $S_\perp$ sometimes coincide gives no indication for an overcorrection.

Figure 7 shows two microphysical/optical model runs for the same cloud, one for the cloud center, the other for the lower edge. Only 0.01% of all particles are assumed to be activated as NAT and to grow when $T < T_{\mathrm{NAT}}$. These simulations clearly illustrate how the low number density of NAT particles governs the uptake kinetics in the cloud preventing equilibrium between the cloud particles on the timescale of cloud development. The value of the HNO_3 hydrate number density is in accordance with our previous analyses of mountain-induced PSCs [*Carslaw et al.*, 1998] and denitrification events [*Waibel et al.*, 1999]. The final values of $S_\parallel$, $S_\perp$, and δ^{Aer} are marked for comparison in Figure 6, showing rather good agreement between the

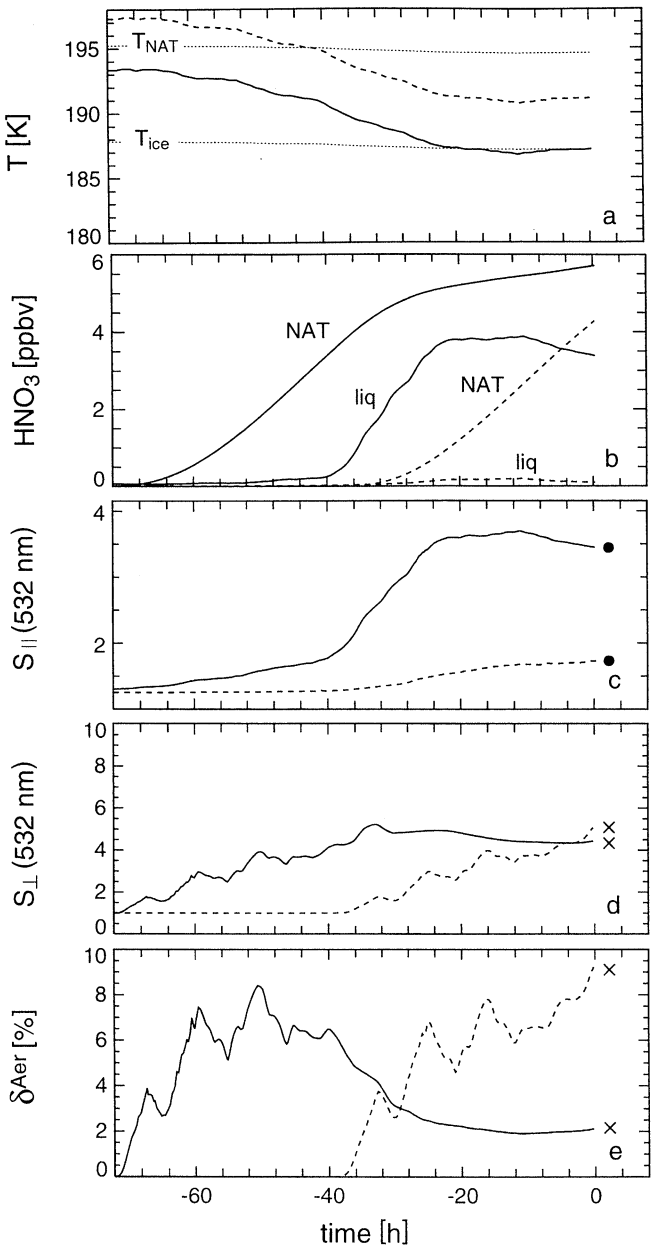

Figure 7. Fully kinetic simulations for the cloud shown in Figure 6. Solid curves denote 3-day European Center for Medium-Range Weather Forecasts (ECMWF) back-trajectory ending at the cloud center (20-km altitude); temperatures have been lowered by 1.3 K to account for a nearby radiosonde measurement. Dashed curves denote same trajectory, but warmer by 4 K referring to lower cloud edge (16.5-km altitude). Initial conditions are as follows: 5 ppmv total H_2O, 10 ppbv total HNO_3, 0.1 ppbv H_2SO_4 condensed in 10 particles cm^{-3} (at 230 K). Only 0.01% of all particles are assumed to nucleate NAT and to grow provided $T < T_{NAT}$. Optical results are based on T matrix calculations for particles with constant aspect ratio 0.85. (a) Temperature development. Dotted lines are NAT coexistence and frost point temperatures. (b) Amount of HNO_3 in liquid (top curves) and NAT particles (lower curves). (c) Total backscatter ratio at 532 nm. (d) Perpendicular backscatter ratio. (e) Aerosol depolarization ratio.

modeled cases and the measurements. However, only two model curves have been considered, and the fine structure of the cloud profile, in particular the remaining sandwich structure in $S_{||}$, cannot be explained in the absence of detailed and accurate temperature and NAT number density information.

5.2. Ny Ålesund Type I PSC Statistics

Finally, we screened the entire Ny Ålesund 1995–1997 data set for type Ib PSCs with and without detectable solid particles. Plate 3 presents all experimental data of the three winters in $(S_{||}, S_{\perp})$ space. Highlighted by red points are measurements belonging to the cloud shown in Figure 6. Plate 3 reveals a substantial number of measurements apparently without solid particles (marked by green points). These are purely liquid clouds. The other measurements indicate the presence of solid particles (marked by blue and red points). As discussed above, these are external mixtures of liquid and solid particles. A vertical solid line at $S_{||} = 1.4$ is shown to suggest the conventional boundary between type Ia ($S_t \leq 1.4$) and type Ib ($S_t \geq 2.5$) PSCs. From Plate 3 it is evident that an appreciable fraction of the type Ib PSCs over Ny Ålesund contain a small fraction of solid particles.

Table 1 presents our new definitions of PSC types based on $S_{\perp}$ and $S_{||}$ alone. The definitions here depend partly also on the sensitivity (detection limit) of the lidar instrument, i.e., on the uncertainty of $S_{\perp}$ and $S_{||}$; we refrained from replacing the quantity $2\,\mathcal{E}(S_{\perp}, S_{||})$ by a fixed number because the uncertainty of a backscatter ratio measurement is not a constant. For rough estimates, $\mathcal{E}(S_{\perp}) = 0.18$ and $\mathcal{E}(S_{||}) = 0.1$ are appropriate. The present definition shows the minimum abundance of coexisting liquid and solid particle PSCs that are clearly above our detection limit. Future measurements with potentially smaller uncertainties might lead to refined PSC type definitions. Note that our type "Ia-enh" is identical to type Ic of *Toon et al.* [2000] and type Id of *Wedekind* [1997], while "mixed phase Ib" is possibly identical to type M of *Rosen et al.* [1997]. For completeness, we give the "type II" definition in terms of $S_{\perp}, S_{||}$ as well; note here that the given values are true only when the ice number density is high ($> 0.5\ cm^{-3}$) and the ice particle radii are $<3\ \mu m$. For large ice particles (synoptic ice clouds) the values can be much smaller; theoretically, ice clouds could then have similar lidar properties $S_{||}, S_{\perp}$ as Ia-enh. The particular numerical constants in the formulas given in Table 1 for $S_{\perp}$ correspond to a minimum aerosol depolarization $\delta^{Aer} = 0.2$ of the solids present: $14 = 0.2/0.0144$. Rescale for lidar systems with other values of the Rayleigh depolarization.

6. Conclusions and Outlook

On the basis of the present analysis, we conclude that the microphysics of polar stratospheric clouds in the

Arctic is more often characterized by nonequilibrium conditions than assumed previously. Not only do rapid temperature fluctuations, as they occur above mountain ranges, strongly influence particle distributions, but even places that are presumably not perturbed by orographic effects lend support to the notion that type I PSC particles are rarely in equilibrium with themselves or with the gas phase. In particular, there is strong indication that particles in type Ia PSCs hardly ever grow to their equilibrium volume and that type Ib PSCs often contain nonequilibrated hydrate particles (see also recent articles by *Shibata et al.*[1999a, b]).

On the basis of the analysis of the perpendicularly polarized backscatter ratio, $S_\perp$, of the Ny Ålesund lidar measurements, we show that type Ib PSCs may occur as purely liquid clouds or may contain solid particles with low number densities and low condensed mass. This is not evident if only total backscatter ratio and depolarizations are analyzed. On the experimental side, such measurements require a careful analysis of polarized quantities, as slight imperfections of the instrument can introduce a systematic bias in the evaluation of $S_\perp$. At the same time, a bias in depolarization ratios can be easily overlooked.

Optical calculations allow us to simulate the basic properties of our data set, if we assume small number densities (1 per liter or less) of rather large nitric acid hydrate particles (mean radius ~2 μm or larger) to coexist with liquid H_2SO_4/H_2O or $HNO_3/H_2SO_4/H_2O$ particles. Apart from the very rarely observed type Ia-enh clouds, in which a large fraction of the total number of particles may become activated as hydrates, there are no PSCs composed entirely of solid particles above T_{ice}. Rather, liquid particles originating from the background aerosol are always present with number densities of the order of 10 cm^{-3}. Hence, even in strongly depolarizing type Ia clouds only a small number of large solid particles may develop. Owing to their importance in stratospheric denitrification and ozone loss, such large HNO_3-containing cloud particles are again of great interest, since particles with radii up to 10 μm and number densities of around 10^{-4} cm^{-3} containing about 2 ppbv of the total available HNO_3 have been discovered in the Arctic [*Fahey et al.*, 2001].

Temperature analyses of solid particle observations are in agreement with the assumption that the particles are composed of NAT, while optical properties of liquid PSCs are in quantitative agreement with the STS theory. Where and how the solid particles form remain open questions. Hypotheses range from nucleation of NAT on ice [*Koop et al.*, 1995], via heterogeneous nucleation on hitherto unknown nuclei [*Drdla*, 1993], to radiation-induced nucleation (similar to galactic cosmic rays causing ice nucleation in cloud chambers [*Anderson et al.*, 1980]). Quantitative answers are required in view of the potential importance of these mechanisms in the context of stratospheric denitrification, which may become an increasingly relevant factor in a colder future stratosphere [*Waibel et al.*, 1999].

Notation

L	lidar ratio = α^{Aer}/β^{Aer}.
n	number concentration.
R_{mod}	median radius of lognormal distribution.
σ	width of lognormal size distribution.
$S_{t,\parallel,\perp}$	backscatter ratio (unpolarized, parallel, perpendicular).
T	absolute temperature.
$\mathcal{E}(X)$	uncertainty of X (standard deviation).
X^{meas}	quantity X not corrected for instrumental polarization bias.
α	extinction coefficient.
α^{Aer}	aerosol extinction coefficient.
β	backscatter coefficient.
β^{Aer}	aerosol backscatter coefficient.
δ^{Aer}	aerosol depolarization.
δ^{Vol}	volume depolarization (bandwidth 10 nm).
δ^{c}	instrumental correction constant.
δ^{Ray}	Rayleigh depolarization.
ϵ	aspect ratio of spheroidal particle.
λ	wavelength.
AWI	Alfred Wegener Institute for Polar and Marine Research.
NAT	nitric acid trihydrate ($HNO_3 \cdot 3\,H_2O$).
NAH	nitric acid hydrates.
SAT	sulfuric acid tetrahydrate ($H_2SO_4 \cdot 4\,H_2O$).
STS	supercooled ternary solution ($HNO_3/H_2SO_4/H_2O$).

Acknowledgments. We wish to thank M. I. Mishchenko for his T matrix scattering algorithms and Thomas Trautmann for implementation and help with that code. We are grateful to Eberhard Reimer (Free University, Berlin), Holger Deckelmann, and Peter von der Gathen (both at AWI, Potsdam) for their back trajectory computations. J.B. greatly appreciates the hospitality of the geophysics and meteorology groups of Adolf Ebel and Fritz M. Neubauer at the University of Cologne, Germany, as well as continued support from AWI Potsdam. Finally, we thank our three referees for unusually thorough reviews, which helped improving the manuscript substantially. Terry Deshler's comments are gratefully acknowledged. Part of this work was funded by the European Communities under contract APE (ENV4-CT95-0143) and the German BMBF under contract 01LO9506. Contribution 1541 of the Alfred Wegener Institute.

References

Aellig, C., *et al.*, Space-born H_2O observations in the Arctic stratosphere and mesosphere in the spring of 1992, *Geophys. Res. Lett.*, *23*, 2325–2328, 1996.

Anderson, R. J., R. C. Miller, J. L. Kassner Jr., and D. E. Hagen, A study of condensation-freezing nucleation of small water droplets in an expansion cloud chamber, *J. Atmos. Sci.*, *37*, 2508–2520, 1980.

Bacmeister, J. T., S. D. Eckermann, A. Tsias, K. S. Carslaw, and T. Peter, Mesoscale temperature fluctuations induced by a spectrum of gravity waves: A comparison of parameterizations and their impact on stratospheric microphysics, *J. Atmos. Sci., 56,* 1913–1924, 1999.

Baumgarten, G., Erste Messungen des Bonner Rayleigh/Mie/Raman-Lidar auf Esrange, Schweden, zur Untersuchung von dynamisch induzierten polaren Stratosphärenwolken im Januar 1997, *Publ IB-97-26,* Univ. of Bonn, Bonn, Germany, 1997.

Beyerle, G., R. Neuber, O. Schrems, F. Wittrock, and B. Knudsen, Multiwavelength lidar measurements of stratospheric aerosols above Spitsbergen during winter 1992-/1993, *Geophys. Res. Lett., 21,* 57–60, 1994.

Beyerle, G., B. P. Luo, R. Neuber, T. Peter, and I. S. McDermid, Temperature dependence of ternary solution particle volumes as observed by lidar in the Arctic stratosphere during winter 1992/1993, *J. Geophys. Res., 102* , 3603–3609, 1997.

Beyerle, G., J. Biele, R. Neuber, and K. Stebel, The lidar data set of polar stratospheric cloud observations at Koldewey-Station, Ny Ålesund, Spitzbergen: An analysis of cloud spatial characteristics, paper presented at *Atmospheric Ozone: Quadrennial Ozone Symposium, Sapporo, Japan, NASDA,* 2000.

Biele, J., Polare stratosphärische Wolken: Lidar-Beobachtungen, Charakterisierung von Entstehung und Entwicklung, *Polarforschung Rep. 303,* Alfred-Wegener-Institut für Polar- und Meeresforschung, Bremerhaven, Germany, 1999.

Biele, J., and G. Beyerle, Polarization lidar: Correction of instrumental effects, *Opt. Express, 7*(12), 427–435, Dec. 4, 2000.

Biele, J., R. Neuber, J. Warming, I. Beninga, P. von der Gathen, K. Stebel, O. Schrems, and J. Rosen, The evolution of polar stratospheric clouds above Spitsbergen in winter 1996/1997, in *Proceedings of the 4th European Symposium on Polar Stratospheric Ozone, Schliersee, Germany, Res. Rep. 66,* edited by N. R. P. Harris, I. Kilbane-Dawe, and G. T. Amanatidis, pp. 99-102, Eur. Comm. Air Pollut., Bruxelles, Belgium, 1997a.

Biele, J., R. Neuber, J. Warming, I. Beninga, P. von der Gathen, J. Notholt, K. Stebel, and O. Schrems, The evolution of stratospheric clouds above Spitsbergen, *J. Aerosol Sci., 28,* Suppl. 1, 423–424, 1997b.

Browell, E. V., C. F. Butler, S. Ismail, P. A. Robinette, A. F. Carter, N. S. Higdon, O. B. Toon, M. R. Schoeberl, and A. F. Tuck, Airborne lidar observations in the wintertime Arctic stratospheric clouds, *Geophys. Res. Lett., 17,* 385–388, 1990.

Burrows, J. P., A. Richter, A. Dehn, B. Deters, S. Himmelmann, S. Voigt, and J. Orphal, Atmospheric remote-sensing reference data from GOME, 2, Temperature-dependent absorption cross sections of O_3 in the 231–794 nm range, *J. Quant. Spectrosc. Radiat. Transfer, 61* , 509–517, 1999.

Carslaw, K. S., B. P. Luo, S. L. Clegg, T. Peter, P. Brimblecombe, and P. J. Crutzen, Stratospheric aerosol growth and HNO_3 gas phase depletion from coupled HNO_3 and water uptake by liquid particles, *Geophys. Res. Lett. 21,* 2479–2482, 1994.

Carslaw, K. S., M. Wirth, A. Tsias, B. P. Luo, A. Dörnbrack, M. Leutbecher, H. Volkert, W. Renger, J. T. Bacmeister, and T. Peter, Particle microphysics and chemistry in remotely observed mountain polar stratospheric clouds, *J. Geophys. Res., 103,* 5785–5796, 1998.

Deshler, T., B. Nardi, A. Adriani, F. Cairo, G. Hansen, F. Fierli, A. Hauchecorne, and L. Pulvirenti, Determining the index of refraction of polar stratospheric clouds above Andoya (69°N) by combining size-resolved concentration and optical scattering measurements, *J. Geophys. Res., 105,* 3943-3953, 2000.

Donovan, D. P., J. A. Whiteway, and A. I. Carswell, Correction for non-linear photon-counting effects in lidar systems, *Appl.Opt., 32,* 6742–6753, 1993.

Drdla, K., Application of a model of PSCs and heterogeneous chemistry, Ph.D. thesis, Univ. of Calif., Los Angeles, 396 pp., 1993.

Fahey, D.W., et al., The detection of large HNO_3 containing particles in the winter Arctic stratosphere, *Science, 291,* 1026–1030, 2001.

Hanson, D. and K. Mauersberger, Laboratory studies of the nitric acid trihydrate: Implications for the south polar atmosphere, *Geophys. Res. Lett., 15,* 855–858, 1988.

Hervig, M. E., K. S. Carslaw, T. Peter, T. Deshler, L. L. Gordley, G. Redaelli, U. Biermann, and J. M. Russell III, Polar stratospheric clouds due to vapor enhancement: HALOE observations of the Antarctic vortex in 1993, *J. Geophys. Res. 102,* 28,185–28,193, 1997.

Klett, J. D., Stable analytical inversion solution for processing lidar returns, *Appl. Opt., 20,* 211–220, 1981.

Klett, J. D., Lidar inversion with variable backscatter/extinction ratios, *Applied Optics, 24,* 1638–1643, 1985.

Koop, T., U. M. Biermann, W. Raber, B. P. Luo, P. J. Crutzen, and T. Peter, Do stratospheric aerosol droplets freeze above the ice frost point?, *Geophys. Res. Lett., 22,* 917–920, 1995.

Koop, T., K. S. Carslaw, and Th. Peter, Thermodynamic stability and phase transitions of PSC particles, *Geophys. Res. Lett., 24,* 2199-2202, 1997.

Meilinger, S.K., T. Koop, B.P. Luo, T. Huthwelker, K.S. Carslaw, P.J. Crutzen and T. Peter, Size-dependent stratospheric droplet composition in lee wave temperature fluctuations and their potential role in PSC freezing, *Geophys. Res. Lett., 22,* 3031–3034, 1995.

Mishchenko, M. I., Light scattering by randomly oriented axially symmetric particles, *J. Opt. Soc. Am., 8,* 871–882, 1991.

Notholt, J., G. Toon, F. Stordal, S. Solberg, N. Schmidbauer, E. Becker, A. Meier, and B. Sen, Seasonal variations of atmospheric trace gases in the high Arctic at 79°N, *J. Geophys. Res., 102,* 12,855–12,861, 1997.

Ovarlez, J., and Ovarlez, H., Stratospheric water vapor content evolution during EASOE, *Geophys. Res. Lett., 21,* 1235–1238, 1994.

Peter, T., Microphysics and heterogeneous chemistry of polar stratospheric clouds, *Annu. Rev. Phys. Chem., 48,* 785–822, 1997.

Poole, L. R., and M. P. McCormick, Airborne lidar observation of Arctic polar stratospheric clouds: Indication of two distinct growth modes, *Geophys. Res. Lett., 15,* 21–25, 1988.

Press, W. H., B. P. Flannery, S. A. Teukolsky, and W. T. Vetterling, *Numerical Recipes - The Art of Scientific Computing,* Cambridge Univ. Press, New York, 1986.

Rosen, J. M., N. T. Kjome, N. Larsen, B. M. Knudsen, E. Kyrö, R. Kivi, J. Karhu, R. Neuber, and I. Beninga, Polar stratospheric cloud threshold temperatures in the 1995–1996 Arctic vortex, *J. Geophys. Res., 102,* 28,195–28,202, 1997.

Schiller, C., A. Engel, U. Schmidt, R. Borchers, and J. Ovarlez, The partitioning of hydrogen species in the Arctic winter stratosphere: Implications for microphysical parameters, *J. Geophys. Res., 101,* 14,489–14,493, 1996.

Shibata, T., Y. Iwasaka, M. Fujiwara, M. Hayashi, M. Nagatani, K. Shiraishi, H. Adachi, T. Sakai, K. Susumi, and Y. Nakura, Polar stratospheric clouds observed by lidar over Spitsbergen in the winter of 1994/1995: Liquid

particles and vertical "sandwich" structure, *J. Geophys. Res., 102,* 10,829–10,840, 1997.

Shibata, T., K. Shiraishi, H. Adashi, Y. Iwasaka, and M. Fujiwara, On the lidar-observed sandwich structure of polar stratospheric clouds (PSCs), 1, Implications for the mixing state of the PSC particles, *J. Geophys. Res., 104,* 21,603–21,611, 1999a.

Shibata, T., K. Shiraishi, H. Adashi, Y. Iwasaka, and M. Fujiwara, On the lidar-observed sandwich structure of polar stratospheric clouds (PSCs), 2, Numerical simulations of externally mixed PSC particles, *J. Geophys. Res., 104,* 21,613–21,619, 1999b.

Shindell, D.T., D. Rind, and O. Lonergan, Increased polar stratospheric ozone losses and delayed eventual recovery owing to increased greenhouse gas concentrations, *Nature, 392,* 589-592, 1998.

Stebel, K., Lidar Beobachtungen stratosphärischer Aerosole in der Arktis über Spitsbergen (79°N, 12°O), Ph.D. thesis, Univ. Bremen, Kiruna, Sweden, 1998.

Stebel, K., R. Neuber, G. Beyerle, J. Biele, P. Scheuch, H. Schuett, P. von der Gathen, and O. Schrems, Lidar observations of polar stratospheric clouds above Spitsbergen, *Advances in Atmospheric Remote Sensing with Lidar,* edited by A. Ansmann, R. Neuber, P. Rairoux, and U. Wandinger, pp. 509-512, Springer-Verlag New York, 1996.

Stein, B., *et al.*, Optical classification, existence temperatures, and coexistence of different polar stratospheric cload types, *J. Geophys. Res., 104,* 23,983–23,993, 1999.

Steinbrecht, W., Lidar measurements of ozone, Aaerosol and temperatures in the stratosphere, *Ph.D. thesis,* York Univ., North York, Ont., Canada, 1994.

Tabazadeh, A., and O. B. Toon, The presence of metastable HNO_3/H_2O solid phases in the stratosphere inferred from ER 2 data, *J. Geophys. Res., 101,* 9071–9078, 1996.

Tabazadeh, A., R. P. Turco, K. Drdla, M. Z. Jacobson, and O.B. Toon, A study of Type I polar stratospheric cloud formation, *Geophys. Res. Lett., 21,* 1619–1622, 1994.

Toon, O. B., E. V. Browell, S. Kinne, and J. Jordan, An analysis of lidar observations of polar stratospheric clouds, *Geophys. Res. Lett., 17,* 393–396, 1990.

Toon, O. B., A. Tabazadeh, E. V. Browell, and J. Jordan, Aerosols and clouds: Analysis of lidar observations of Arctic polar stratospheric clouds during January 1989, *J. Geophys. Res., 105,* 20,589–20,616, 2000.

Tsias, A., A. Prenni, K. S. Carslaw, M. A. Tolbert, and T. Peter, Freezing of polar stratospheric clouds in orographically-induced strong warming events, *Geophys. Res. Lett., 24,* 2303–2306, 1997.

Tsias, A., *et al.*, Aircraft lidar observations of an enhanced type Ia polar stratospheric clouds during APE-POLECAT, *J. Geophys. Res., 104,* 23,961–23,969, 1999.

Vömel, H., M. Rummukainen, R. Kivi, J. Karhu, T. Turunen, E. Kyrö, J. Rosen, N. Kjome, and S. Oltmans, Dehydration and sedimentation of ice particles in the Arctic stratospheric vortex, *Geophys. Res. Lett., 24,* 795–798, 1997.

Waibel, A. E., T. Peter, K. S. Carslaw, H. Oelhaf, G. Wetzel, P. J. Crutzen, U. Pöschl, A. Tsias, E. Reimer, and H. Fischer, Arctic ozone loss due to denitrification, *Science, 283,* 2064–2069, 1999.

Warneck, P., Chemistry of the Natural Atmosphere, Academic, San Diego, Calif., 1988.

Wedekind, C., Lidar-Untersuchungen von Bildung und Dynamik polarer Stratosphärenwolken in der Arktis, Ph.D. thesis, Free Univ. of Berlin, Berlin, Germany, 1997.

World Meteorological Organization (WMO), Scientific assessment of ozone depletion, Rep. 37, Global Ozone Res. and Monit. Project, Geneva, 1994.

G. Beyerle, GeoForschungsZentrum, Telegrafenberg A17, D-14473 Potsdam, Germany. (gbeyerle@gfz-potsdam.de)

J. Biele (corresponding author), Deutsches Zentrum für Luft- und Raumfahrt e.V. (DLR), Institut für Raumsimulation, D-51170 Köln, Germany. (jens.biele@dlr.de)

K. S. Carslaw, School of the Environment, University of Leeds, Leeds LS2 9JT, England. (carslaw@env.leeds.ac.uk)

B. Luo and T. Peter, Laboratorium für Atmosphärenphysik, Swiss Federal Institute of Technology (ETH), CH-8093 Zürich, Switzerland. (luo@atmos.umnw.ethz.ch; tom@atmos.umnw.ethz.ch)

R. Neuber, Alfred Wegener Institute for Polar and Marine Research, Research Unit Potsdam, Telegrafenberg A43, D-14473 Potsdam, Germany. (neuber@awi-potsdam.de)

A. Tsias, Airsys ATM, Robert-Bosch-Straße 25, D-63225 Langen, Germany. (athanassios.tsias@de.airsysatm.thomson-csf.com)

(Received March 31, 2000; revised January 25, 2001; accepted February 4, 2001.)